Xiangmeng Meng, Antoni Artinov, Marcel Bachmann, Ömer Üstündağ, Andrey Gumenyuk, Michael Rethmeier

The detrimental molten pool narrowing phenomenon in wire feed laser beam welding and its suppression by magnetohydrodynamic technique

Citation details
Meng, X., Artinov, A., Bachmann, M., Üstündağ, Ö., Gumenyuk, A., & Rethmeier, M. (2022). The detrimental molten pool narrowing phenomenon in wire feed laser beam welding and its suppression by magnetohydrodynamic technique. In International Journal of Heat and Mass Transfer (Vol. 193, p. 122913). Elsevier BV. https://doi.org/10.1016/j.ijheatmasstransfer.2022.122913.

The detrimental molten pool narrowing phenomenon in wire feed laser beam welding and its suppression by magnetohydrodynamic technique

Xiangmeng Meng[a,*], Antoni Artinov[a], Marcel Bachmann[a], Ömer Üstündağ[a], Andrey Gumenyuk[a], Michael Rethmeier[b,a]

[a] BAM Federal Institute for Materials Research and Testing, Unter den Eichen 87, 12205 Berlin, Germany

[b] Technische Universität Berlin, Institute of Machine Tools and Factory Management, Pascalstraße 8-9, 10587 Berlin, Germany

Corresponding author: xiangmeng.meng@bam.de

Abstract

Element transport in the wire feed laser beam welding (WFLBW) is directly determined by the molten pool shape and thermo-fluid flow therein. In this paper, an untypical molten pool profile, i.e., elongated at its top and bottom but narrowed at the middle, is found experimentally by real-time metal/glass observation and numerically by multi-physical modeling. *Ex-situ* X-ray fluorescence element mapping is used to characterize the element dilution status in the fusion zone. For the first time, the detrimental influence of the molten pool narrowing on the element transport is identified and discussed, combining the experimental and numerical results. A magnetohydrodynamic technique is utilized to suppress the narrowing, aiming at a more homogenous element distribution. It is found that due to the interaction of the two dominant circulations from the top and bottom regions of the molten pool, a low-temperature region is formed. It leads to an untypical growth of the mushy zone, narrowing the molten pool in the middle region. Its detrimental effect on material mixing is non-negligible considering the direct blocking effect on the downward flow and the premature solidification at the middle region. The Lorentz force from a transverse oscillating magnetic field can change the flow pattern into a single-circulation type. The downward transfer channel is widened, and its premature solidification is prevented because the low-temperature-gradient region is mitigated. This paper provides a supplementary reason regarding the common issue of insufficient material mixing during LBW, and a promising technique to optimize the process.

Keywords: thermo-fluid flow, element transport, laser beam welding, magnetohydrodynamics, multi-physical modeling

1. Introduction

During the last decades, the deep penetration laser beam welding process (LBW) has been

attracting more and more attention from both the academic and industrial fields. Compared with the traditional arc welding process, the LBW shows some incomparable advantages, e.g., precise, and highly localized heat input, better penetration capacity, and lower residual distortion. However, the utilization of the small laser spot and the corresponding high energy density may lead to drawbacks during the practical application of LBW. The small dimension of the laser spot makes the weld seam sensitive to the assembly tolerances of the workpiece. The vigorous evaporation may result in a serious loss of important alloying elements, e.g., Mg or Zn in Al alloy, which may deteriorate the final weld properties [1].

A common solution for the issue described above is the introduction of filler material, mostly in the form of a filler wire, into the traditional LBW process, also known as the wire feed laser beam welding (WFLBW). During WFLBW, a part of the laser energy is absorbed by the filler wire, leading to its melting and further transport into the molten pool [2]. The stream of the liquid filler metal which is much larger than the laser spot significantly reduces the gap tolerance sensitivity. By choosing a filler wire with proper chemical composition, important alloying elements can be supplemented to the molten pool, thus achieving a better control over the metallurgical process, and eliminating the potential defects formation. However, the molten pool with narrow and deep geometry and high solidification rate causes difficulties in the downward transfer of the filler metal. Often, the filler material accumulates on the upper part of the final weld, undermining the homogeneity of the weld properties [3].

The molten pool during the partial penetration LBW is typically elongated at the upper region, driven by the recoil pressure and the Marangoni shear stress, whereas it is relatively short in the bottom region. This type of molten pool profile has been confirmed in numerous studies [4-7]. The solidification starts at the bottom and lateral boundary of the molten pool, and the solid-liquid (S/L) interface moves toward the top surface and the central line [8]. Recently, a different type of molten pool shape was observed both experimentally and numerically [9-11]. The molten pool boundary is elongated at both the top region and bottom region. The molten pool in the middle, resultantly, is significantly narrowed. This untypical narrowing is usually but not necessarily accompanied by the occurrence of the bulge phenomenon which is characterized by an elongation of the bottom region [12]. The bulge phenomenon may occur independently from the narrowing studied in the present paper [13]. To the best of the authors' knowledge, little research has been reported on the clarification of the formation conditions of the untypical molten pool narrowing as well as its influence on the flow pattern therein. However, it can be easily foreseen that once formed during WFLBW, the narrowed region may further deteriorate the downward transport of the filler metal.

Since the first attempt by Kern *et al.* [14], in which an external magnetic field was applied to suppress humping defects in high-speed LBW, the magnetohydrodynamic (MHD) technology has shown more and more importance to improve the capacity of the traditional LBW. Different beneficial effects can be produced by choosing a magnetic field with proper position, strength, frequency, and orientation, such as electromagnetic support against gravity to eliminate sagging of the weld seam [15], electromagnetic exclusive force to suppress porosity [16], and refinement of the grain structure [17,18].

It has also been found that the material mixing in the WFLBW can be enhanced by an oscillating magnetic field. The work of Gatzen suggested that during WFLBW of Al alloys, the Si from the filler wire was mixed more uniformly when employing a coaxial alternating magnetic field with a frequency below 25 Hz [19]. In the authors' previous study, a transverse high-frequency magnetic field was imposed from the top side of the workpiece during WFLBW of austenitic steel with filler wire of nickel-based Inconel 625 alloy. An apparent downward flow driven by the induced Lorentz force was formed in the molten pool, achieving a homogenous Ni distribution successfully. Additionally, the grain structure was also refined compared to the common WFLBW due to the direct mechanical dendrite fragmentation [20]. Üstündag *et al.* found that the material mixing during hybrid laser-arc welding, which has a close physical essence with the WFLBW, was as well improved radically by applying an oscillating magnetic field from the bottom side [21].

Although the benefits from the magnetic field on the LBW process have been well recognized, the underlying physics occurring in the molten pool remain unclear. Considering the difficulties in the direct measurement of thermal, optical, and electrical signals in the molten pool, only a few experimental observations have been reported so far to reveal the influence of the magnetic field on the molten pool behavior. Gatzen *et al.* applied an in-situ X-ray measurement with tracing particles to observe the metal flow during LBW under the influence of the oscillating magnetic field [22]. Recently, the metal/glass technique was more commonly utilized to observe the molten pool dynamics in the longitudinal section, in which the unmelted and adiabatic glass works as a symmetrical boundary [9, 23,24]. The geometries of the keyhole and molten pool can be captured through the transparent quartz glass by a high-speed camera together with an additional illumination system. It was found by this technique that the magnetic field can sufficiently influence the keyhole stability, the laser absorption, and the final penetration depth [25-27]. The glass may serve well as a symmetrical boundary for the heat transfer and fluid flow, but inevitably it leads also to changes in the multiple reflections path of the laser beam and the electrical condition. This deviation should be carefully evaluated and discussed in detail.

As the improvement of the computational capacity, the multi-physical modeling which takes the full coupling between thermo-fluid flow and magnetic field, namely MHD, provides great potential to obtain the quantitative and comprehensive descriptions of molten pool behavior under the influence of the magnetic field. Bachmann *et al.* developed a three-dimensional steady-state MHD model with a predefined keyhole profile [28-30]. The influences of static and alternating magnetic fields on the molten pool behavior and the formation of sagging defect were investigated. The onset of the bulging phenomenon, without accompanying narrowed region in the middle, was reported in the study as well [30]. However, the impact of the magnetic field on this phenomenon was not further discussed. The influence of the magnetic field orientation was studied numerically by Chen *et al.* using a 3D transient model with a fixed keyhole [31]. This model was further developed to calculate the thermoelectric currents and the thermoelectric-magnetic effects in the molten pool [32]. Recently, more sophisticated MHD models were developed, in which the volume-of-fluid (VOF) or level-set method was implemented to track the highly dynamic keyhole geometry [33,34]. Different beneficial effects of the LBW with a magnetic field, including sagging defect elimination by the electromagnetic support and grain refinement by the thermoelectric current effect, were investigated more deeply.

The enhancement of the material mixing in the molten pool from a low-frequency coaxial magnetic field was explained numerically by Gatzen *et al.* using a MHD model with a fixed keyhole [35]. The inhomogeneity problem of the element distribution was moderated, but a spatial periodicity of the concentration remained due to the periodic Lorentz force. A multi-physical model considering the transient keyhole evolution was developed for the electromagnetic stirring enhanced wire feed laser beam welding (EMS-WFLBW) in the authors' recent work [36-39]. The influence of the electromagnetic stirring from a transverse high-frequency magnetic field on the molten pool behavior, the keyhole dynamics, and the element distribution were revealed. It should be noted that the molten pool in the above studies shows a common shape, i.e., elongated at the upper region and relatively short at the bottom. The problem of inhomogeneous element distribution basically originates from the steep molten pool shape and the high solidification rate which are inevitable during deep-penetration LBW.

In the present study, an untypical narrowing phenomenon in the middle of the molten pool during WFLBW is identified by real-time metal/glass observation and multi-physical modeling. The material mixing is characterized by an *Ex-situ* X-ray fluorescence (XRF) element mapping. By combining the experimental and numerical results, the formation mechanism of the molten pool narrowing is analyzed and its resulting detrimental effect on the element transport is discussed. By introducing an external oscillating magnetic field, the narrowed region is successfully suppressed,

providing a better material mixing in the final weld seam. The influences of the Lorentz force on the thermo-fluid flow in the molten pool, the suppression of the molten pool narrowing, and the element transport are studied as well.

2. Mathematical modeling

A three-dimensional MHD model coupled with VOF algorithm and element transport equation is developed to calculate the temperature and velocity fields, the keyhole dynamics, the Ni distribution, and the electromagnetic phenomena during WFLBW and EMS-WFLBW. Since the model is based on previous works from the authors, here the key physical features of the welding process will be formulated concisely, emphasizing the improvements of the model. Further details of the numerical setup can be found in the authors' previous works [3,37,38].

2.1 Governing equations

The transient free surface evolution is tracked by the VOF algorithm, which is governed by the following equation:

$$\frac{\partial F}{\partial t}+\nabla\cdot\left(\vec{v}F\right)=S_F \quad (1)$$

where F is the volume fraction and S_F is the volume source from the filler metal. The free surface, more precisely the interface between the steel and the Ar gaseous phase, is located within the cells with a volume fraction between 0 and 1. It is worth noting, that only the spatial distribution of the volume fraction can be obtained by Eq. (1), which makes the free surface geometry found by the VOF method not naturally explicit. The piecewise linear interface calculation (PLIC) method is implemented to reconstruct the free surface geometry [40].

The transport phenomena can be calculated by solving the conservation equations of mass, momentum, energy, and chemical species, which are defined as follows:

$$\nabla\cdot\vec{v}=\frac{m_{\mathrm{w}}}{\rho} \quad (2)$$

$$\rho\left(\frac{\partial\vec{v}}{\partial t}+\vec{v}\cdot\nabla\vec{v}\right)=-\nabla p+\mu\nabla^2\vec{v}-\mu K\vec{v}+m_{\mathrm{w}}\vec{v}_{\mathrm{w}}+\vec{S}_{\mathrm{m}} \quad (3)$$

$$\rho\left[\frac{\partial h}{\partial t}+\left(\vec{v}\cdot\nabla\right)h\right]=\nabla\cdot\left(k\nabla T\right)+h_{\mathrm{w}}+S_q \quad (4)$$

$$\frac{\partial F_{\mathrm{s}}\rho_{\mathrm{s}}w_{\mathrm{Ni}}}{\partial t}+\nabla\cdot\left(F_{\mathrm{s}}\rho_{\mathrm{s}}\vec{v}w_{\mathrm{Ni}}-F_{\mathrm{s}}D_{\mathrm{Ni}}\nabla w_{\mathrm{Ni}}\right)=S_{\mathrm{Ni}} \quad (5)$$

In the mass equation (Eq. (2)), ρ is the density, m_w is the mass source from the filler wire. In the momentum equation (Eq. (3)), t is the time, p is the pressure, μ is the dynamic viscosity, $\vec{v}_w$ is the velocity of the molten filler metal, K is the Carman–Kozeny equation coefficient, which is responsible for the deceleration of the liquid in the mushy zone, and $\vec{S}_{\mathrm{m}}$ is the momentum source. Due to the application of the VOF method, all surface forces are converted into localized volumetric forces using the continuum surface force method [41]. The physical mechanisms that contribute to the $\vec{S}_{\mathrm{m}}$ term include recoil vapor pressure, surface tension, and Marangoni stress. The influence of the shielding gas is neglected. In the energy equation (Eq. (4)), T is the temperature, k is the thermal conductivity, h is the enthalpy, h_w is the energy source from the molten filler metal, and S_q is the additional energy source term. Similar to the $\vec{S}_{\mathrm{m}}$ term, the laser heat flux and the thermal dissipation are converted and implemented in the S_q term. In the element transport equation (Eq. (5)), w_{Ni} is the weight percentage of Ni, F_{s} is the steel volume fraction, D_{Ni} is the diffusion coefficient of Ni in iron, and S_{Ni} is the Ni source term from the filler wire.

A magnetic induction equation, rather than the full set of Maxwell equations, is solved for the MHD behavior. This method does not require including the electromagnet in the simulation domain. Instead, the experimentally measured external magnetic field $\vec{B}_0$ is implemented as input data, as given below:

$$\frac{\partial \vec{b}}{\partial t}+\left(\vec{v}\cdot\nabla\right)\vec{b}=\frac{1}{\mu_{\mathrm{m}}\sigma_{\mathrm{e}}}\nabla^2\vec{b}+\left(\left(\vec{B}_0+\vec{b}\right)\cdot\nabla\right)\vec{v}-\left(\vec{v}\cdot\nabla\right)\vec{B}_0 \quad (6)$$

where μ_{m} is the magnetic permeability, σ_{e} is the electrical conductivity, $\vec{b}$ is the induced magnetic field from the liquid flow, and the temporal variation of $\vec{B}_0$ in the case where a transient magnetic field is applied. For the simplification, the solidified 304 stainless steel is assumed to keep a perfectly austenitic microstructure, thus μ_{m} is set to 1. The thermo-magnetic effect is neglected in the current study because the induced eddy current in the applied magnetic parameters is one order of magnitude higher than the thermo-magnetic current [34].

By using $\vec{B}_0$ and $\vec{b}$, the induced Lorentz force which is the driving force from the MHD technique to adjust the molten pool behavior can be calculated as:

$$\vec{j}=\frac{1}{\mu_m}\nabla\times\left(\vec{B}_0+\vec{b}\right) \quad (7)$$

$$\vec{F}_{\mathrm{L}}=\vec{j}\times\vec{B}=\vec{j}\times\left(\vec{B}_0+\vec{b}\right) \quad (8)$$

where $\vec{j}$ is the current density and $\vec{F}_{\mathrm{L}}$ is the Lorentz force.

2.2 Welding models

An accurate description of the laser energy on the keyhole wall is crucial for an accurate calculation of the highly dynamic molten pool behavior during LBW. In the authors' previous studies, a ray tracing method was implemented to calculate the multiple reflections of the laser beam and the Fresnel absorption. The laser beam was discretized by a sufficient number of sub-rays, and each sub-ray has its own location-dependent energy density and initial incidence angle [42]. In addition, the influence of the filler wire on the allocation of the laser energy and the blocking-out of the filler wire on the laser beam profile were considered empirically [38].

However, the applied ray-tracing method has its limitations and leads to certain deviations in accuracy. Since the free surface geometry calculated with the VOF approach is not explicit, it leads to difficulties in calculating the exact reflection point of the laser beam on the keyhole wall. Usually, a compromised criterion is used to find the reflection position. A cell is identified as a "reflection cell" when the following equation is satisfied:

$$D_{\mathrm{ray}} \le \sqrt{3}\Delta/2 \quad (9)$$

where D_{ray} is the distance between the cell center and the incident ray and Δ is the cell size.

The cell size of the model (0.2 mm), however, is quite comparable with the diameter of the laser spot (0.56 mm). It may lead to a non-negligible inaccuracy during calculating the multiple reflection paths of the laser sub-ray, especially when the keyhole front wall is steep and is nearly parallel to the laser beam, as shown in Fig. 1(a).

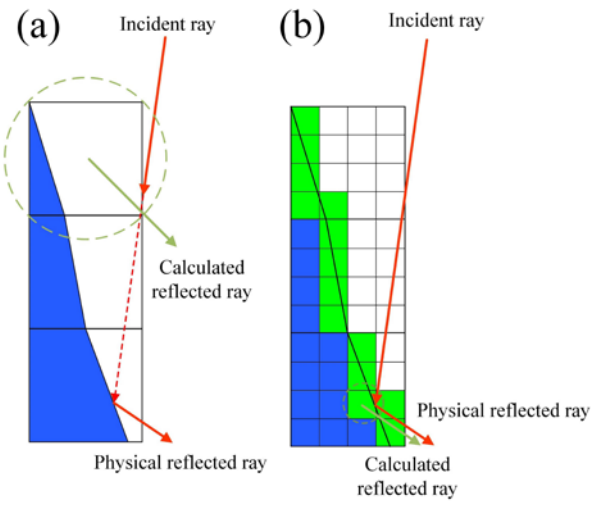

Fig. 1 Schematic of the ray-tracing method: (a) conventional ray-tracing method, (b) ray-tracing method with a local grid refinement

A direct strategy to improve the ray-tracing method is the reduction of the cell size, but it will also result in a significant increment of the computational intensity. Hereby, a local grid refinement algorithm is developed to improve the accuracy of the ray-tracing method [43], meanwhile maintaining the current computational cost. The potential reflection cell is further divided into finer secondary virtual cells. These virtual cells are used for the calculation of the multiple reflections but are not involved in the CFD computation.

According to the PLIC method, the distance between the cell center and the free surface is unique once the cell has a certain F and gradient of F, i.e., the normal vector of the free surface $\vec{n} = \nabla F = \left(n_x, n_y, n_z\right)$. By taking the cell center as the origin, the free surface within this cell, which is assumed to be a plane, can be expressed as:

$$n_x x + n_y y + n_z z = D_{\text{free}} \quad (10)$$

where D_{free} is the distance from the free surface to the cell center, n_x, n_y, and n_z are the x, y, z components of the normal vector. D_{free} can be calculated analytically or numerically using F and $\vec{n}$ [40].

In the first iteration of the search algorithm, Eq. (9) is employed to identify all the potential reflection cells. Subsequently, the selected cells are divided into virtual cells with a typical cell size of 0.05 mm, and the virtual cell on the free surface can be easily confirmed using Eq. (10). In Fig. 1(b), the green cells represent the virtual cells laying on the free surface, and the blue cells represent the steel cells, which are not considered in the calculation of the reflection point. In the second iteration of the search algorithm, the reflection point is determined among the virtual cells on the free surface with a much smaller Δ in Eq. (9), which may improve the accuracy of the ray-tracing method.

Two benchmarks are conducted to test the two ray-tracing methods using a predefined keyhole geometry as shown in Fig. 2. The predefined geometry has the typical and important keyhole features for deep penetration laser beam welding, e.g., steep shape and small humps on the front wall [44]. For the ray-tracing method without local refinement algorithm, the laser beam is absorbed by the upper convex part of the keyhole. In the contrast, it reaches the bottom of the keyhole when using a virtual cell refinement, which is more consistent with the physics behind the reflection and absorption phenomena. It should be pointed out that the energy is not always absorbed by the upper convex part even if the conventional ray-tracing method is used. The convex part will be instantaneously eliminated by the recoil pressure, and the laser spot also reaches the keyhole bottom within

microseconds. Nevertheless, the local refinement algorithm may provide better physical consistency and a more accurate description of the laser energy on the keyhole wall.

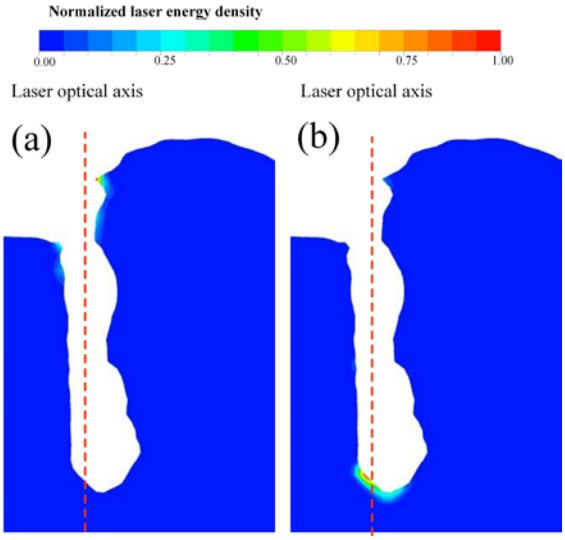

Fig. 2 Benchmarks of the ray-tracing algorithm: (a) ray-tracing method without a local grid refinement, (b) ray-tracing method with a local grid refinement

The temperature-dependent recoil pressure p_r from the metal evaporation, which is the dominant driving force for the keyhole formation, is calculated as [45]

$$p_r = \frac{AB}{\sqrt{T}} \exp\left(-\frac{m\Delta L_v}{R_g T} \right) \quad (11)$$

where m is the molar mass, ΔL_v is the evaporation latent heat, R_g is the ideal gas constant, and A and B are material-dependent evaporation coefficients, which are taken as 0.55 and 3.9×10^{12} kg/m·s^2 for pure iron, respectively. The influence of other alloying elements on evaporation is neglected in this study.

The normal capillary pressure p_{ca} is the main driving force to balance the recoil pressure, determining the keyhole geometry. Meanwhile, the tangential Marangoni shear stress τ_{ma} from the temperature-dependent surface tension is also involved.

$$p_{ca} = \gamma\kappa \quad (12)$$

$$\tau_{ma} = \frac{\partial\gamma}{\partial T}\frac{\partial T}{\partial \vec{s}} \quad (13)$$

where κ is the curvature and $\vec{s}$ is the tangential vector of the keyhole surface.

Excluding the Lorentz force, two volumetric forces, i.e., the hydrostatic pressure F_h and the buoyancy F_b are considered in the source term $\vec{S}_m$.

$$\vec{F}_h = \rho\vec{g} \quad (14)$$

$$\vec{F}_b = -\beta\rho(T - T_L)\vec{g} \quad (15)$$

where $\vec{g}$ is the gravity acceleration, β is the thermal expansion coefficient, and T_L is the liquidus temperature.

All the material properties used in the above governing equations and physical models are the averaged values based on the mass fractions of the base metal and the filler metal. The properties are listed in Table 1.

Table 1 Thermophysical properties of materials used in the model [46-48].

Properties (Unit)	304 steel	NiCr20Mo15 alloy
Density (kg/m^3)	6900	8440
Thermal conductivity (W/m·K)	T-dependent	T-dependent
Specific heat (J/kg·K)	T-dependent	575
Viscosity (Pa·s)	T-dependent	T-dependent
Surface tension coefficient (N/m)	T-dependent	-
Melting latent heat (kJ/kg)	274	227
Liquidus temperature (K)	1727	1623
Solidus temperature (K)	1673	1563
Emissivity	0.4	0.4
Expansion coefficient (1/K)	1.2×10^{-5}	1.6×10^{-5}
Electric conductivity (S/m)	T-dependent	7.46×10^{5}
Magnetic permeability (H/m)	1.26×10^{-6}	1.26×10^{-6}

2.3 Boundary conditions and computational domain

The computational domain with the dimensions of 30 mm × 8 mm × 12 mm is meshed. The central region is uniformly meshed into 0.2 mm hexahedron cells, and the cell size grows gradually in the zone far away from the molten pool. Corresponding to the experimental condition, a 10 mm thick solid steel phase and a 2 mm thick gaseous Ar phase are initialized. The laser beam and the filler wire are kept stationary during the calculation, and a velocity inlet and a pressure outlet are set to achieve the movement of the workpiece, as shown in Fig. 3.

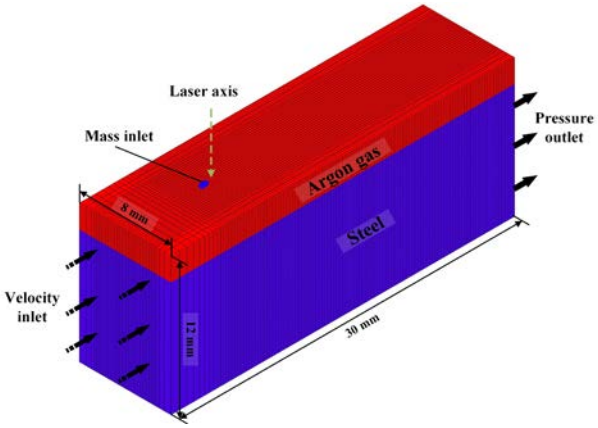

Fig. 3 Schematic and mesh of the computational domain

The thermal boundary condition on the keyhole wall can be written as:

$$k\frac{\partial T}{\partial \vec{n}} = q_L - h_c(T - T_0) - \sigma\varepsilon_{\mathbf{r}}(T^4 - T_0^4) - \rho v_{evp}\Delta L_v + q_{plume} + q_{recond} \quad (16)$$

where q_{L} is the laser heat influx on the keyhole wall from the ray-tracing method, h_{c} is the convective heat loss coefficient, σ is the Stefan-Boltzmann constant, ε_{r} is the emissivity and v_{evp} is the free surface recession speed due to evaporation.

The momentum boundary condition on the keyhole wall is expressed as follows:

$$-p + 2\mu\frac{\partial v_{\mathrm{n}}}{\partial \vec{n}} = -p_{\mathrm{r}} - p_{\mathrm{vapor}} + p_{\mathrm{ca}} \quad (17)$$

$$-\mu\frac{\partial v_{\mathrm{t}}}{\partial \vec{n}} = \tau_{\mathrm{ma}} + \tau_{\mathrm{vapor}} \quad . (18)$$

The high-temperature and high-velocity metal vapor may also bring non-negligible influences on the keyhole dynamics, which are considered empirically according to the work of Muhammad *et al* [49]. In Eq. (16) - (18), p_{vapor} and τ_{vapor} are the stagnation pressure and the shear stress from the impact of the high-velocity vapor, respectively. q_{plume} is the additional heating effect from the vapor plume and q_{recond} is the release of the evaporation latent heat due to the vapor's re-condensation.

2.4 Numerical implementation

The transport equations, the VOF equation, and the magnetic induction equation were solved by the universal CFD software ANSYS Fluent 19.5. The convection-diffusion equations were spatially discretized by the second order upwind method. The Pressure-Implicit with Splitting of Operators (PISO) algorithm was applied for the pressure-velocity coupling. The reference case of WFLBW was first calculated from 0 s to 1.5 s, and the obtained data were used as the initial condition for the subsequent calculation of MHD cases (1.5 s - 3.0 s). The computations were performed on a high-

performance computing cluster with 88 CPU cores and 768 GB RAM. Every 1.0 s real time welding simulation required a clock time of 60 hours. Multiple simulation cases with different electromagnetic parameters were conducted to provide a preliminary parametric study, as given in Table 2.

Table 2 Electromagnetic parameters used in the investigation

Case	Magnetic flux density (mT)	Frequency (kHz)	Angle with respect to transverse direction (deg)	Approach
Ref	-	-	-	Num. & Exp.
1	250	3.6	10	Num. & Exp.
2	250	3.6	40	Num. & Exp.
3	250	1.8	10	Num.
4	190	3.6	10	Num.
5	125	3.6	10	Num.

3. Experimental setup

The base metal and the filler material were chosen as AISI 304 stainless steel and NiCr20Mo15 alloy, respectively, in which a distinct difference of the Ni content existed (9 % vs. 64 %). The substrate had the dimensions of 200 mm × 60 mm × 10 mm and the diameter of the filler wire was 1.1 mm. An IPG YLR 20000 laser system was used as the laser source. The wavelength of the laser was 1.07 μm, and the laser beam radius in the focal plane was 0.28 mm, which was located 3 mm beneath the substrate top surface. A butt joint configuration with a technical zero gap was conducted, and the substrate was irradiated by a vertical beam from a fixed laser head. A laser power of 6.5 kW was used, and the welding speed was set to 1.3 m/min. The leading filler wire was fed with a feeding rate of 2.1 m/min and had a 33° angle with respect to the substrate surface. The shielding gas of pure Argon was provided behind the laser spot with a flow rate of 20 L/min.

A specially designed electromagnet in which a resonant circuit was integrated was employed to produce sufficiently high magnetic flux density and frequency (up to 250 mT and 3600 Hz, respectively) [16]. The electromagnet was fixed 2 mm above the substrate surface. The experimental system of EMS-WFLBW is shown schematically in Fig. 4(a). A Hall sensor was used to measure the spatial distribution of the magnetic flux density in cold metal condition. The measured data were subsequently applied in the multi-physical model as the initial condition [37].

A configuration of steel and quartz glass was performed to observe the real-time molten pool

profile without filler material [50], as shown in Fig. 4(b). A high-speed camera (Fastcam 1024) operating at the frame rate of 3000 Hz was used to capture the molten pool shape from the metal/glass interface. The camera was equipped with a bandpass filter at 808±1.5 nm to suppress the interference of intensive light from incident laser radiation and vapor/plasma on the imaging signal. The optical axis of the lens was parallel with the welding plane and perpendicular to the welding direction.

The transverse and longitudinal sections of the weld specimen were etched by a V2A etchant (100 ml H_2O, 100 ml HNO_3, and 10 ml HCl) after they were mechanically cut, ground and polished. XRF mapping was conducted to measure the Ni content on the longitudinal section to characterize the material mixing. The scanning spot size was 20 μm and the measurement time per spot was 50 ms.

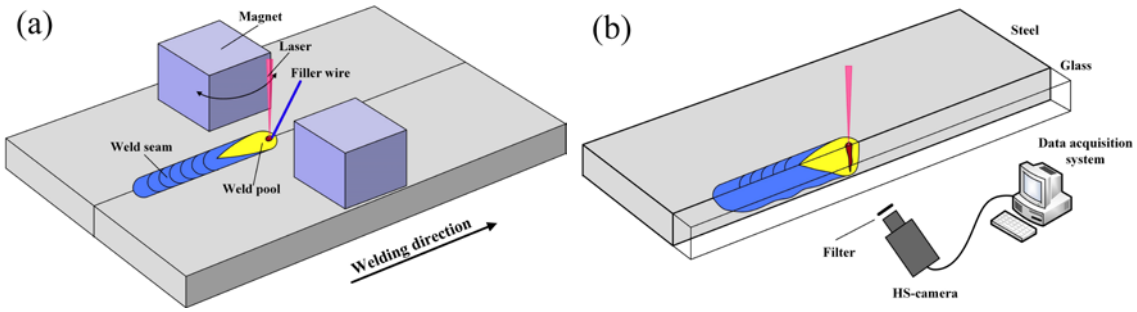

Fig. 4 Schematic of the experimental setup: (a) EMS-WFLBW, (b) metal/glass observation

4. Results and discussion

4.1 Model validation

Fig. 5 gives the comparison of the fusion line shape on the cross-section between the experimental and numerical results for Case Ref, Case 1, and Case 2. The detailed values and the relative errors are listed in Table 3. The model shows high accuracy in predicting the weld penetration but gives larger deviations in the prediction of weld width. The deviations may be due to the empirical filler wire model in which the physical interaction between the laser beam and the filler wire is not considered.

The variation of the penetration depth caused by the magnetic field may come from two aspects. First, the Lorentz force influences the keyhole dynamics and the backward flow of the liquid metal, which in turn changes the energy absorption and the energy allocation [37]. Second, the melting front of the filler wire is also probably affected by the magnetic field. The vibration of the melting front may increase the dissipation ratio of the laser energy [38].

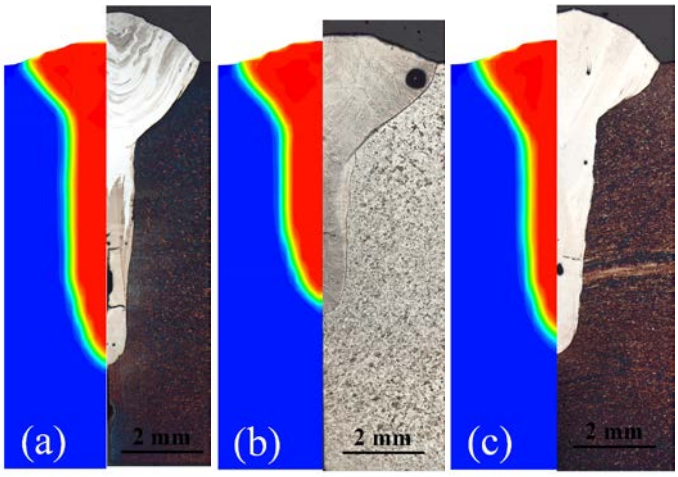

Fig. 5 Comparison of the fusion line shapes between the numerical and experimental results: (a) Case Ref, (b) Case 1, (c) Case 2.

Table 3 The numerical and experimental values of the weld size

	Penetration			Weld width			Middle weld width		
	Num. (mm)	Exp. (mm)	Error (%)	Num. (mm)	Exp. (mm)	Error (%)	Num. (mm)	Exp. (mm)	Error (%)
Ref.	7.3	7.4	-1.3	3.8	4.6	-17.4	1.5	1.4	+7.1
Case 1	5.8	6.1	-4.9	4.4	5.6	-21.4	1.6	1.3	+23.0
Case 2	6.7	7.2	-6.9	4.2	5.0	-16.0	1.4	1.6	-12.5

To further validate the model, the calculated Ni distributions in the longitudinal section are compared with the XRF-measured results in Fig. 6. As shown in Fig. 6 (a) and Fig. 6 (b), the Ni concentrates in the upper part of the final weld in WFLBW. The Ni-rich zone and the Ni-poor zone are sharply separated by a narrow transition region. After an oscillating magnetic field (250 mT, 3.6 kHz, 10 deg) is applied, the downward transport of the filler metal is apparently enhanced, resulting in an improved element dilution, as seen in Fig. 6(c) and (d). However, a perfectly uniform distribution has not been achieved. The XRF scanning in the longitudinal section shows a periodic spiking distribution of Ni, which is also reproduced by the MHD model. Nevertheless, there is a relatively larger error between the numerically predicted spike distance and the experimental value. When the magnetic field angle changes from 10 deg to 40 deg, the material mixing is not visibly improved, as shown in Fig. 6(f). A small amount of filler metal is still brought to the molten pool by the Lorentz force, which is also predicted successfully by the proposed model. Thus, it can be

concluded that the established MHD model can provide an accurate prediction of the element distribution.

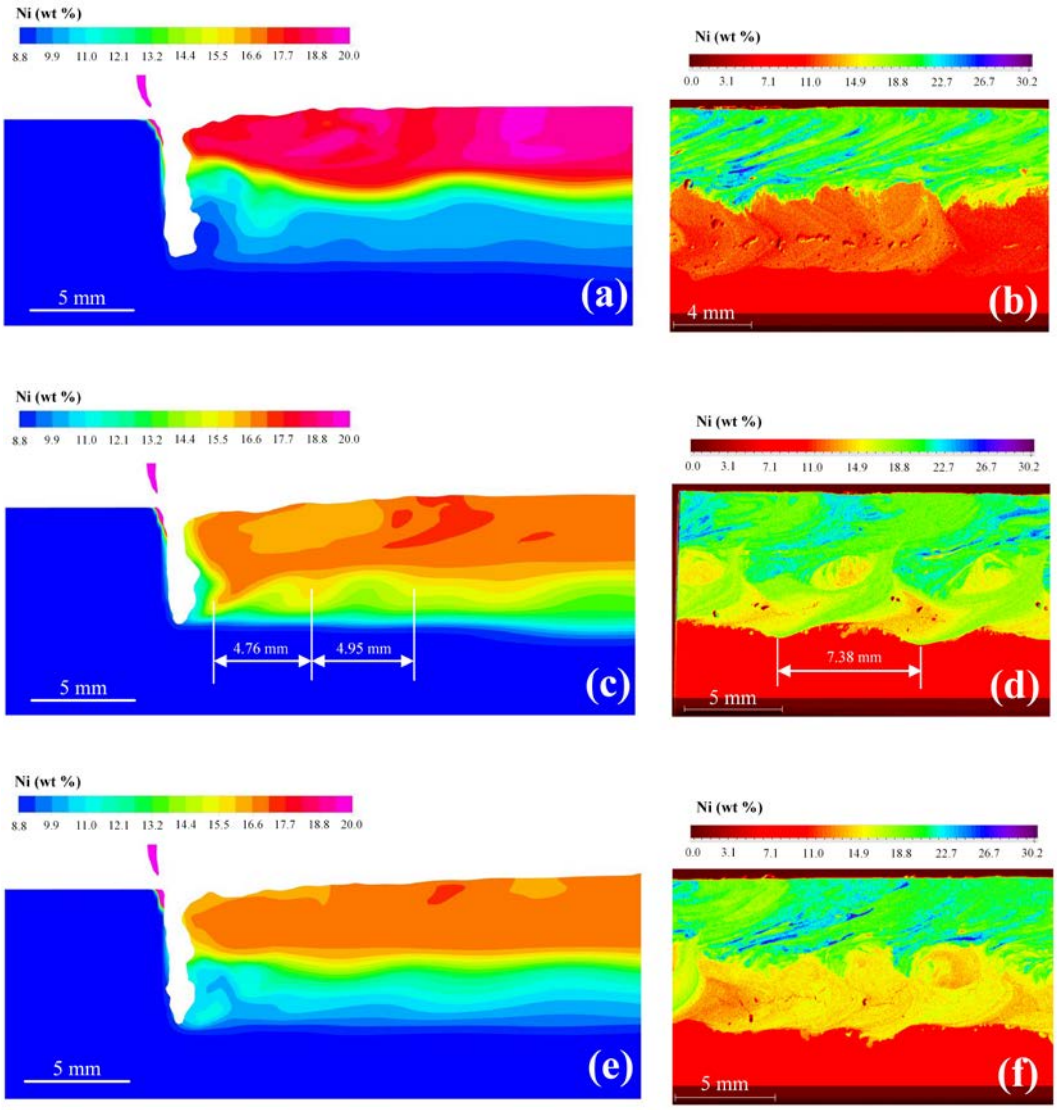

Fig. 6 Calculated and XRF-measured Ni distribution on the longitudinal section: (a) and (b) from Case Ref, (c) and (d) from Case 1, (c) and (f) Case 2

4.2 Formation mechanism of the narrowed region

The formation procedure of narrowed region is shown in Fig. 7, where the solidus and liquidus lines are highlighted by black curves. At t = 0.38 s, the upper circulation dominates the molten pool flow, in which a downward trend can be observed in the longitudinal section. The bottom circulation is comparatively minor, and the flowing direction is alternately clockwise or counterclockwise. Therefore, the molten pool maintains its typical shape at the initial stage of the process. During t =

0.45s - 0.50 s, the bottom circulation develops, and its flowing direction keeps counterclockwise. The molten pool starts to narrow in the middle region. As t = 0.56 s, the narrowed region has fully developed, and the molten pool is segmented by it. The liquid metal at the upper region shows a flow along the horizontal direction, leading to a hindered mass transfer between the upper and bottom regions.

There are two predominant circulations in the fully developed molten pool. In the upper region, the liquid metal flows backward along the free surface, driven by the recoil pressure and the Marangoni stress. The stream turns near the middle region and flows forward in the longitudinal section. This circulation contributes to the elongated profile of the molten pool and the sufficient material mixing in the upper region. The liquid metal near the bottom of the keyhole flows backward and upward along with the S/L interface, and subsequently toward the keyhole rear wall. A confluence of the two circulations is found in the middle region in the thickness direction where the untypical narrowing occurs.

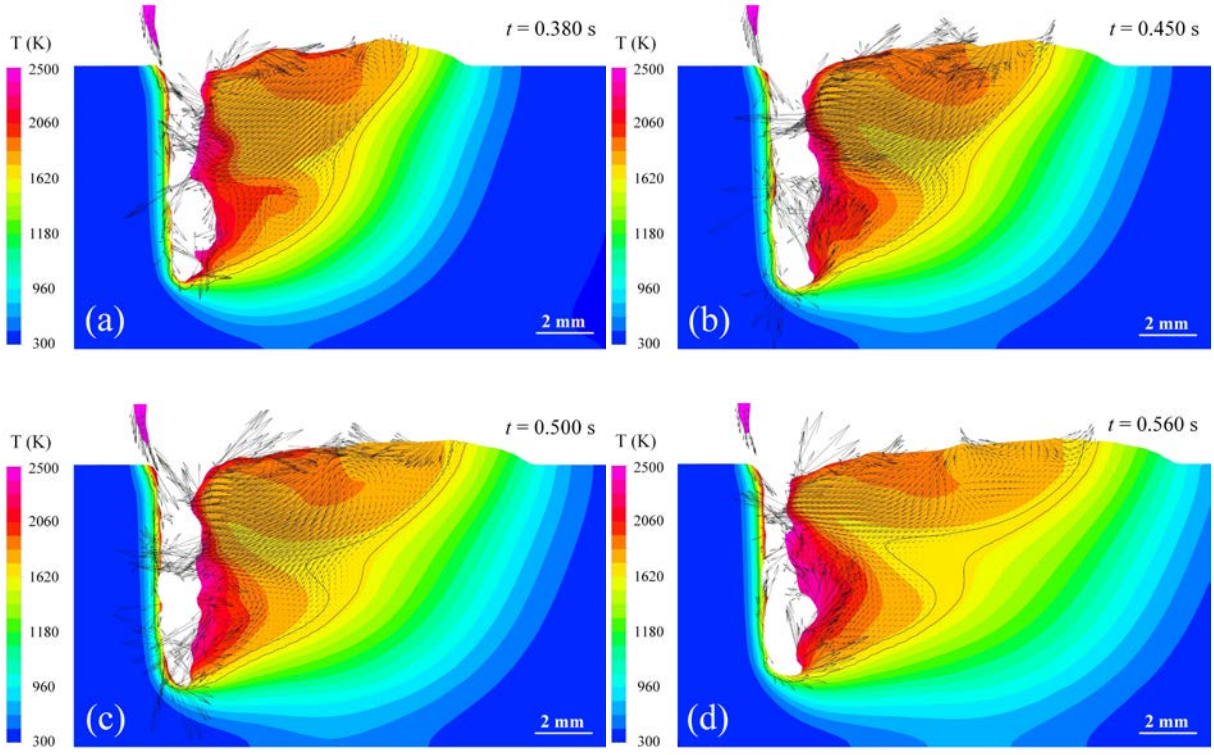

Fig. 7 The formation procedure of molten pool narrowing in Case Ref at: (a) t = 0.38 s, (b) t = 0.45 s, (c) t = 0.50 s, (a) t = 0.56 s.

The images of the molten pool profile from the metal/glass observation are shown in Fig. 8. Currently, it is a compromised way to validate the existence of the narrowed region experimentally since no filler wire can be added in the proposed metal/glass setup. If the laser spot center is located at the metal/glass interface, the symmetrical section of the molten pool is expected to be observed.

As shown in Fig. 8(a), the area with the highest brightness can be considered as the keyhole with high-temperature metal vapor or plasma inside. There are two strong vortexes in the top and bottom regions and a noticeable narrowed region in the middle of the molten pool, which shows similarity with the numerical results in Fig. 7(d). The narrowing phenomenon can be more clearly exhibited when the laser spot moves 0.5 mm toward the steel side, as seen in Fig. 8(b). A longitudinal section which is 0.5 mm away from the symmetrical plane can be captured equivalently. A dark area where the flow can be rarely identified, namely a solid or semisolid area, forms in the middle region, whereas the top and bottom of the molten pool remain liquid. This image also implies that the molten pool is narrowed not only in the longitudinal but also in the transverse direction.

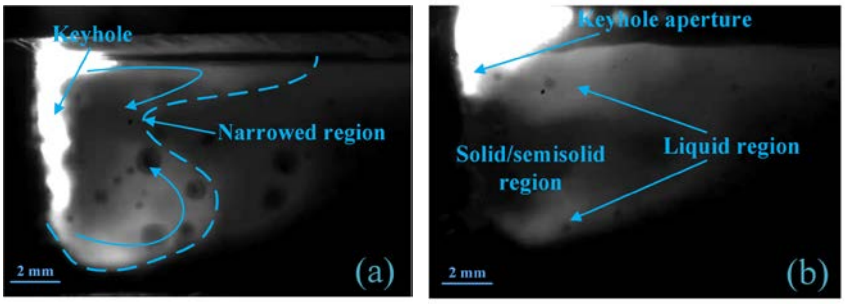

Fig. 8 Molten pool profile observed by the metal/glass experiment: (a) laser spot at metal/glass interface (y=0 mm), (b) laser spot shifted by y = 0.5 mm to the steel side

For the partial penetration LBW, the available research suggests that generally either the upper circulation [7,51,52] or the lower circulation [5, 53, 54] may dominate the molten pool flow. Both flow patterns will produce a typical molten pool shape, i.e., elongated at the top and relatively short at the bottom. The velocity field in Fig. 7, however, shows that the two circulations have similar intensities. The laser energy is directly absorbed by the free surface of the keyhole. Hence the keyhole wall can be considered as an equivalent heat source. Since the Peclet number of the molten pool is larger than 500, the heat transfer from the high-temperature keyhole surface to the comparatively cold liquid metal is dominated by the advective transport rather than the diffusive transport. As the liquid metal stream leaves the vicinity of the keyhole, its enthalpy is gradually transferred into the surrounding liquid material and meanwhile dissipated into the solid workpiece or the surrounding atmosphere. The middle region is the end position for both circulations, implying that it receives the least energy from the keyhole.

It can also be identified from Fig. 7(d) that the solidus boundary has relatively inapparent feature of narrowing. The liquidus boundary, on the contrary, is significantly narrowed in the middle region, resulting in a mushy zone thickness up to 3.5 mm. Excluding the influence from the chemical

composition, e.g., constitutional supercooling, the geometry of the S/L interface is determined by the mechanical gouging effect and the temperature gradient ahead [55]. When the liquid flow is vertical to the solidification direction, it may show a strong gouging effect on the S/L interface. However, the liquid metal in the middle region flows principally parallel to the solidification direction, thereby the mechanical gouging can be considered negligible.

For a molten pool reaching quasi-stable state, the energy entering through the liquidus boundary should be equal to the energy leaving the S/L region to achieve thermal equilibrium. By neglecting the metal flow in the mushy zone and assuming a linear variation of G along the solidification direction in the mushy zone, the problem can be simplified into a one-dimensional thermal model. The thermal balance can be written as:

$$k_{\mathrm{l}} G_{\mathrm{l}} \approx k_{\mathrm{mu}} \frac{2\left(T_{\mathrm{L}} - T_{\mathrm{S}}\right)}{\delta_{\mathrm{mu}}} \quad (19)$$

where k_{l} is the thermal conductivity at the liquidus temperature, G_{l} is the temperature gradient at the liquidus boundary, k_{mu} is the averaged thermal conductivity in the mushy zone, and δ_{mu} is the mushy zone thickness. The Eq. (19) shows that the mushy zone thickness increases with G decreasing.

The temperature gradient varies typically between 2×10^5 K/m - 3×10^5 K/m in the area in front of the liquidus boundary. However, it is noteworthy that a low-temperature-gradient region is formed at the confluent area of the two circulations (the narrowed area), in which the temperature gradient is only 2×10^4 K/m - 3×10^4 K/m, see Fig. 9. By substituting the typical values into Eq. (19) (k_{l} = 33 W/m·K, k_{mu} = 31 W/m·K, $G_{\mathrm{l}} = 2.5 \times 10^4$ K/m), the mushy zone thickness is calculated as 4.1 mm. In comparison, the numerical result is approximately 3.2 mm.

The result from the simplified one-dimensional model shows an acceptable agreement with the numerical outcome, implying that the model captures the main physical feature for the formation of the narrowed region. Therefore, it can be inferred that the formation of the low-temperature-gradient region directly leads to the untypical narrowing.

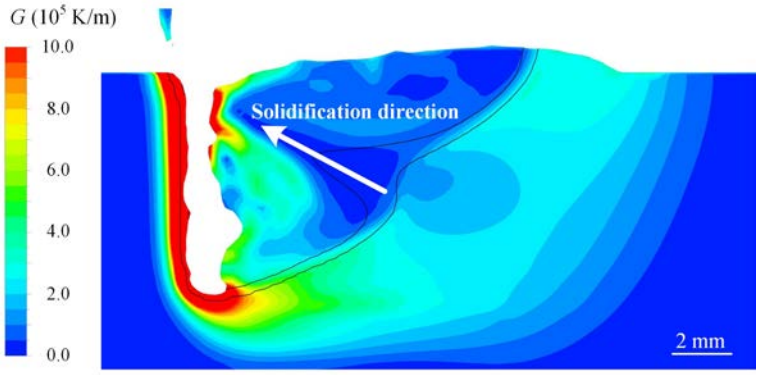

Fig. 9 Temperature gradient in the longitudinal section for Case Ref at t=0.56 s

4.3 Detrimental effect from the narrowing phenomenon

The available research has well recognized that insufficient mixing in the WFLBW is a common problem even if the molten pool has a normal shape without a narrowed region [20, 36, 37]. In the current study, the untypical narrowing may lead to further deterioration of the element homogeneity. A time-averaged z velocity component (1.2 s - 1.5 s) in the longitudinal section is contoured in Fig. 10(a) to provide better visualization of the downward/upward transfer of the filler metal. The liquid metal shows a positive component of the z velocity component in the region near the rear keyhole wall (line AB). The z velocity component can reach up to +0.05 m/s in the bottom region, but it decreases dramatically to nearly zero after flowing across the narrowed region because of the blocking effect, as shown in Fig. 10(b).

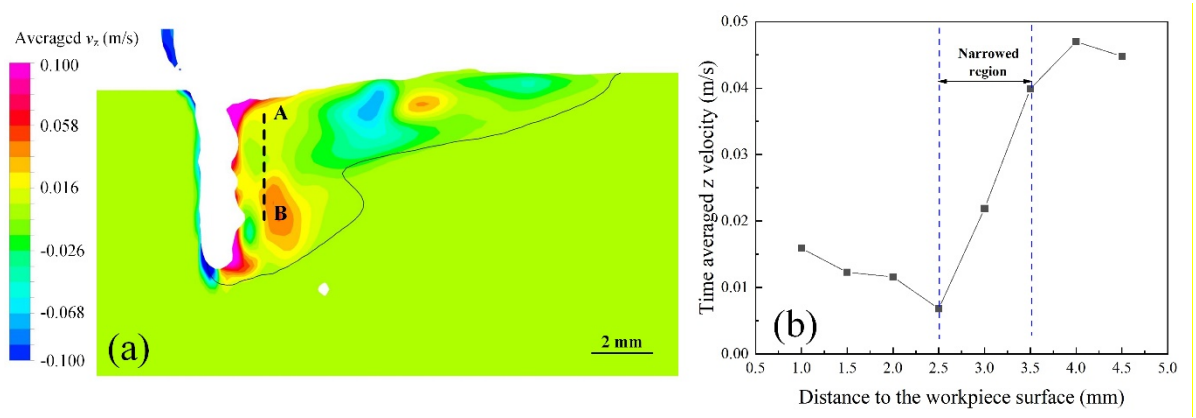

Fig. 10 Time-averaged z velocity component: (a) on longitudinal section from Case Ref, (b) along line AB.

For the typical molten pool shape without narrowing, the solidification sequence starts at the region near the fusion line, and the S/L interface moves toward the region near the central line, which can also be found in numerous publications [8,50,56,57]. Hereby, the downward transfer channel remains open during the whole solidification procedure. Once the narrowed region forms, the premature solidification in the transfer channel occurs at the position of x = 19 mm (3 mm from the laser center), as given in Fig. 11. At the position of x = 18 mm, the middle region has solidified completely, preventing the downward transport of the filler metal.

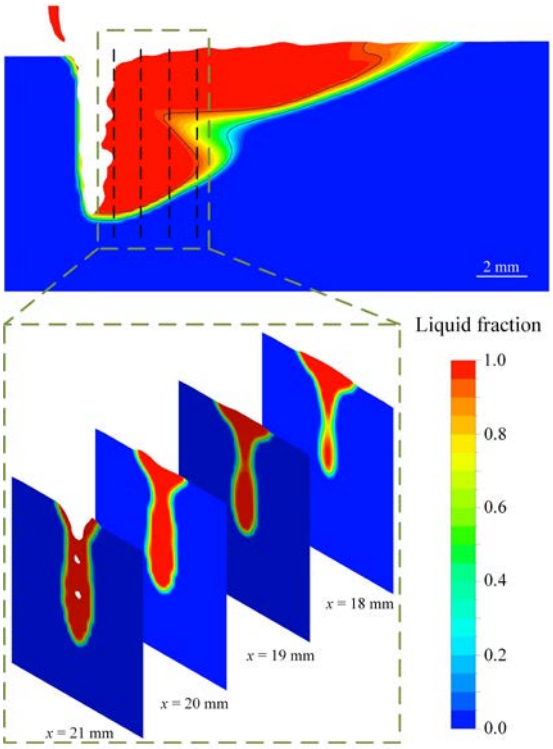

Fig.11 Premature solidification caused by the narrowing of the molten pool

4.4 Suppression of narrowing by MHD technique

A transverse oscillating magnetic field applied from the top side of the workpiece produces a time-averaged downward Lorentz force with a magnitude of 10^5 N/m^3 in the current electromagnetic parameter range. It enhances the backward flow along the molten pool surface as well as the downward flow in the longitudinal section [20,37]. The magnetic field with different strength, frequency, and orientation may produce different influences on the molten pool behavior, and correspondingly different extent of suppression on the narrowing. This chapter focuses on a parametric study of magnetic variables under a representative set of welding parameters causing the narrowing phenomenon. The complex relationship between the welding parameters and magnetic parameters is not further discussed.

Considering that Case 1 has the most uniform element distribution among the current magnetic parameters, it is expected to show the most apparent suppression of the narrowing phenomenon. Compared with Case Ref, the molten pool in Case 1 is elongated from 16.8 mm to 19.6 mm, and the molten pool depth decreases from 7.5 mm to 5.9 mm. The average temperature of the keyhole rear wall shows a reduction from 2450 K to 2300 K. The narrowed region is almost eliminated, more specifically, the untypically thick mushy zone in the middle region is diminished under the induced Lorentz force, from 3.5 mm to 0.7 mm, as shown in Fig. 12.

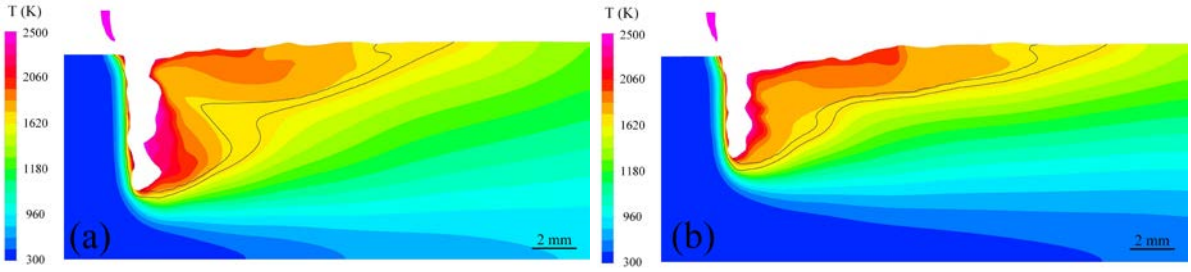

Fig. 12: Calculated temperature fields in the longitudinal section: (a) Case Ref, (b) Case 1.

The time-averaged *x* velocity component on the top surface is provided in Fig. 13. In Case Ref, the liquid metal flows backward along the lateral sides of the molten pool with an average velocity of 0.2 m/s, which contributes to the formation of the upper circulation. The backward flow in Case 1 is significantly accelerated by the Lorentz force and reaches velocities of up to 0.4 m/s. It leads directly to the elongation of the molten pool. Additionally, more energy is transferred from the vicinity of the keyhole to the tail part of the molten pool, leading to the decrease of both keyhole temperature and penetration depth [37].

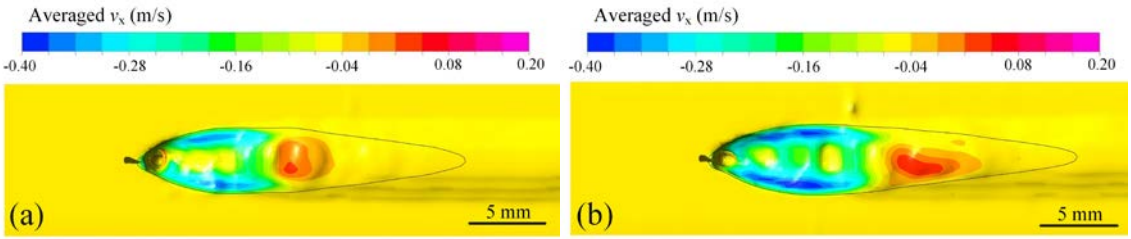

Fig. 13 Time-averaged x velocity components on the top surface: (a) Case Ref (1.2 s - 1.5 s), (b) Case 1 (2.7 s - 3.0 s)

The time-averaged *z* velocity component in the longitudinal section for Case 1 is shown in Fig. 14. The liquid metal on the keyhole rear wall has a time-averaged upward velocity larger than 0.1 m/s, which is consistent with the Case Ref. It indicates that the effect of the Lorentz force is masked by the strong recoil pressure on the keyhole wall. However, the liquid metal shows a downward flow in the longitudinal section in the area relatively far away from the keyhole rear wall. The time-averaged z component velocity is around -0.05 m/s. This flow pattern is directly beneficial for the downward transport of the filler metal, improving the mixing in the final weld.

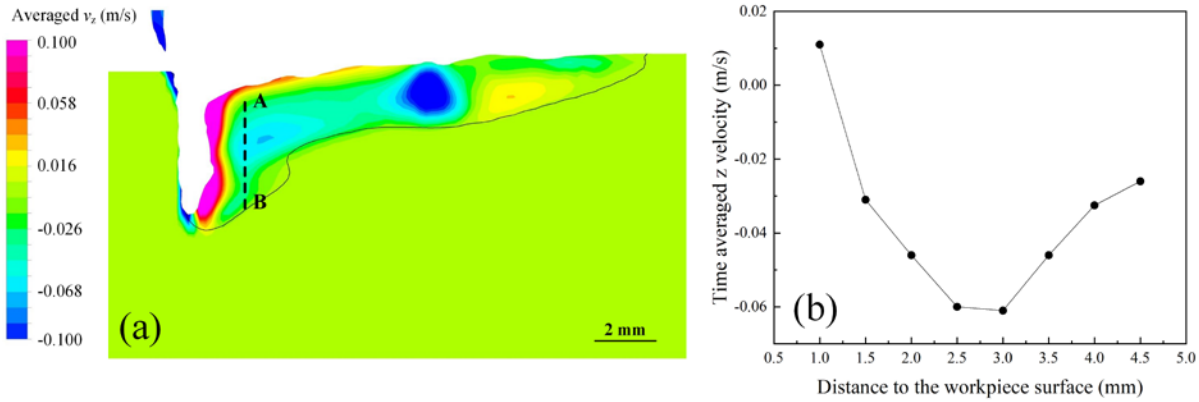

Fig. 14 Time-averaged z velocity components: (a) in the longitudinal section from Case 1, (b) along the line A-B

The slides of the different cross-sections in Fig. 15 show that the molten pool solidifies in a common sequence. No premature solidification in the middle region occurs, thus the downward transfer channel remains open. The suppression of the molten pool narrowing can be explained from two aspects: the temperature gradient in front of the liquidus boundary and the mechanical gouging effect from the liquid flow. Firstly, the two-circulation flow pattern is inhibited by the Lorentz force, and only one circulation dominates the molten pool flow. In this case, more energy is brought from the keyhole region to the middle region. Therefore, the temperature gradient in front of the liquidus boundary there increases from 2×10^4 K/m - 3×10^4 K/m to 8×10^4 K/m - 10×10^4 K/m, comparing Fig. (9) and Fig. 15(b). By substituting $G_l = 9 \times 10^4$ K/m into Eq. (19), the δ_{mu} of 1.2 mm is obtained. In comparison, the numerically calculated value is 0.7 mm. The analytical result has the right order of magnitude, indicating that the change of the temperature gradient mainly contributes to the elimination of the narrowing. However, it shows a relatively larger error which comes from neglecting the mechanical gouging effect. The liquid metal flows vertically to the solidification direction, producing a stronger gouging effect on the S/L interface, which results in a thinner mushy zone.

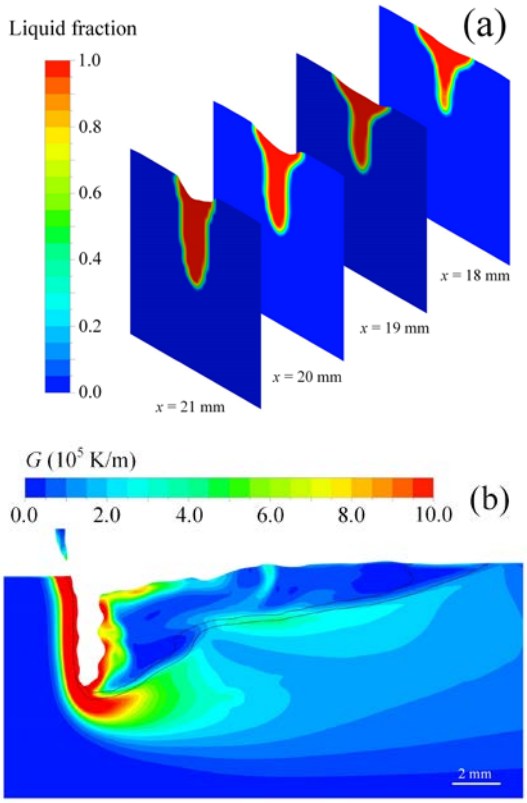

Fig. 15 Influence of the MHD effect in Case 1: (a) solidification sequence; (b) Temperature gradient in the longitudinal section at t=2.50 s

When a magnetic field of 40 deg is applied (Case 2), the counterclockwise circulation at the bottom region is suppressed, but not fully eliminated as in Case 1. It leads to a mushy zone thickness of 2.2 mm in the middle region and a moderate narrowing phenomenon can still be found, as shown in Fig. 16(a). It can be explained that a magnetic field with a larger angle (with respect to the transverse direction) will produce a stronger stirring on the upper region of the molten pool, but it attenuates faster along the thickness direction due to the stronger skin effect [38]. The downward flow at the upper region of the molten pool is enhanced by the Lorentz force, resulting in a maximum value of 0.05 m/s. Since the narrowed region still exists, the downward stream is attenuated dramatically from 0.05 m/s to nearly zero after flowing across the region (see Fig. 16(b)), inhibiting the material mixing. Furthermore, the premature solidification of the downward transfer channel is postponed but still not avoided. The combined detrimental effects lead to insufficient mixing, which is confirmed experimentally and numerically as seen in Fig. 6(e) and (f).

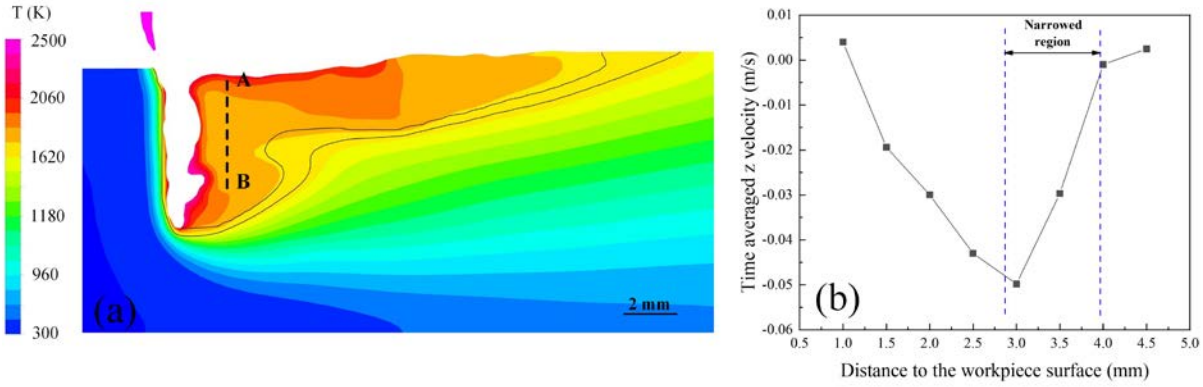

Fig. 16 Calculated molten pool behavior in Case 2: (a) temperature field in longitudinal section, (b) time-averaged *z* velocity component along the line A-B

The oscillating magnetic field with lower frequency generates smaller eddy current, thus smaller Lorentz force, because of the slower temporal variation of magnetic flux density. However, it confronts less skin effect. By using the equation $\delta_{\text{skin}} = \left(\pi \mu_{\text{m}} \sigma_{\text{e}} f\right)^{-1/2}$, the skin depth for the magnetic field of 1800 Hz in Case 3 is estimated as 10.8 mm, and in Case 2 it is below 7.5 mm. This means that the Lorentz force in Case 3 can reach deeper regions of the molten pool, namely it is distributed more uniformly in the molten pool. As shown in Fig. 17(a), the mushy zone thickness decreases to a minor level of 1.4 mm. A downward flow with a maximum value of 0.02 m/s is formed, which is lower than the velocity in Fig. 17(b) for Case 2, but the downward flow shows a slower attenuation when it flows across the narrowed region, since the mushy zone thickness is further decreased. Compared with Case 2, the averaged Ni increment at the molten pool bottom increases from 2.9 % to 3.5 %.

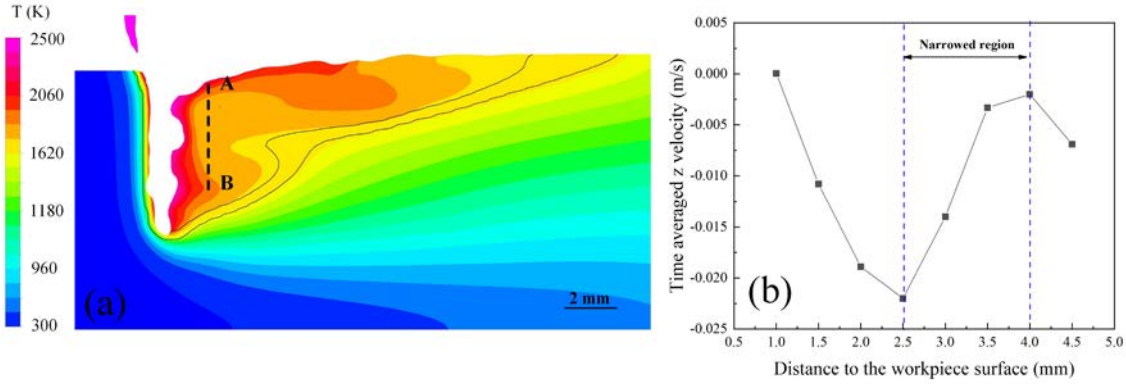

Fig. 17 Calculated molten pool behavior in Case 3: (a) temperature field in longitudinal section, (b) time-averaged *z* velocity component along the line A-B

Based on the above analysis, the dimensionless mushy zone thickness δ_{mushy} in the middle region can be considered as an appropriate index for the characterization of the severity of the narrowing. It is defined as

$$\delta_{mushy} = w_{mushy} / w_{WP} \quad (20)$$

where w_{mushy} is the thickness of the mushy zone, and w_{WP} is the width of molten pool at the middle region. Higher δ_{mushy} means more serious molten pool narrowing. The influence of the magnetic flux density on δ_{mushy} and the averaged Ni content at the weld bottom are shown in Fig. 18. When a magnetic field below 125 mT is applied, the Lorentz force cannot provide an apparent suppression on the detrimental narrowed region, whereby the Ni increment with respect to the base metal increases only from 2.2 % to 2.4 % compared to the Case Ref. When the magnetic flux density increases from 125 mT to 250 mT, the dimensionless mushy zone thickness decreases dramatically from 0.39 to 0.18. It means that both the direct blocking effect caused by the narrowed region and the premature solidification are inhibited, thus the Ni increment reaches up to 5.7 %.

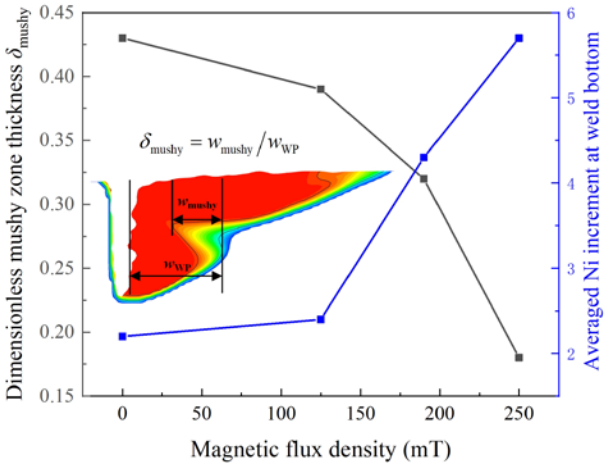

Fig. 18 Influence of the magnetic flux density on the dimensionless mushy zone thickness and the averaged Ni content

5. Conclusions

In the current study, a combination of multi-physical modeling and experiments is presented to identify and study an untypical narrowing phenomenon, occurring at the middle of the molten pool, during WFLBW. The detrimental effect of the narrowed region on the material mixing is evaluated. A MHD technique is introduced to suppress the narrowing and to achieve a better element homogeneity. The suppression mechanism is further discussed. The main conclusions drawn can be summarized as follow:

(1) The detrimental narrowing phenomenon may occur when the molten pool has two dominant circulations at the top and bottom regions. A low-temperature-gradient region is formed under this unique heat transfer pattern, which leads to the untypical growth of the mushy zone, and correspondingly, the narrowing of the molten pool.

(2) The narrowing phenomenon results in a direct blocking effect on the material transfer between the top and bottom regions. Furthermore, the narrowing causes the premature solidification of the molten pool in the middle region, which closes the downward transfer channel completely.

(3) The molten pool narrowing can be suppressed or eliminated when a transverse oscillating magnetic field is applied effectively. The liquid metal flows downward driven by the Lorentz force, thus changing the main flow pattern in the molten pool from two-circulation to a single-circulation type. The low-temperature-gradient region is mitigated, and the mushy zone is significantly thinned. The molten pool will not solidify prematurely in the middle region once the narrowed region is fully suppressed.

(4) The presented parametric study shows that increasing magnetic flux density, decreasing magnetic field angle (with respect to the transverse direction), and increasing frequency produce better suppression of the detrimental narrowing, resulting in a more homogenous element distribution.

Acknowledgment

This work is funded by the Deutsche Forschungsgemeinschaft (DFG, German Research Foundation) – project Nr. 416014189 (BA 5555/6-1) and Nr. 411393804 (BA 5555/5-1).

References

[1] A. Dilthey, A. Goumeniouk, V. Lopota, G. Turichin, E. Valdaitseva, Development of a theory for alloying element losses during laser beam welding, J. Phys. D-Appl. Phys. 34 (1) (2001), 81.

[2] M. J. Torkamany, A. F. Kaplan, F. M. Ghaini, M. Vänskä, A. Salminen, K. Fahlström, J. Hedegård, Wire deposition by a laser-induced boiling front, Opt. Laser Technol. 69 (2015) 104-112.

[3] X. Meng, A. Artinov, M. Bachmann, M. Rethmeier, Numerical study of additional element transport in wire feed laser beam welding, Procedia CIRP 94 (2020) 722-725.

[4] S. Katayama, Y. Kawahito, M. Mizutani, Elucidation of laser welding phenomena and factors affecting weld penetration and welding defects, Phys. Procedia (2010) 5 9-17.

[5] Y. Kawahito, Y.Uemura, Y. Doi, M. Mizutani, K. Nishimoto, H. Kawakami, S. Katayama, Elucidation of the effect of welding speed on melt flows in high-brightness and high-power laser

welding of stainless steel on basis of three-dimensional X-ray transmission in situ observation, Weld. Int. 31(3) (2017) 206-213.
[6] L. Huang, X. Hua, D. Wu, F. Li, Numerical study of keyhole instability and porosity formation mechanism in laser welding of aluminum alloy and steel, J. Mater. Process. Technol. 252 (2018) 421-431.
[7] S. Pang, L. Chen, J. Zhou, Y. Yin, T. Chen, A three-dimensional sharp interface model for self-consistent keyhole and weld pool dynamics in deep penetration laser welding, J. Phys. D-Appl. Phys. 44 (2) (2011) 025301.
[8] W. Tan, Y. C. Shin, Multi-scale modeling of solidification and microstructure development in laser keyhole welding process for austenitic stainless steel, Comput. Mater. Sci. 98 (2015) 446-458.
[9] H. Wang, M. Nakanishi, Y. Kawahito, Dynamic balance of heat and mass in high power density laser welding, Opt. Express 26 (5) (2018) 6392-6399.
[10] S. Muhammad, S. W. Han, S. J. Na, A. Gumenyuk, M. Rethmeier, Numerical investigation of energy input characteristics for high-power fiber laser welding at different positions, Int. J. Adv. Manuf. Tech. 80 (5) (2015) 931-946.
[11] Y. Feng, X. Gao, Y. Zhang, C. Peng, X. Gui, Y. Sun, X. Xiao, Simulation and experiment for dynamics of laser welding keyhole and molten pool at different penetration status, Int. J. Adv. Manuf. Tech. 112(7) (2021) 2301-2312.
[12] A. Artinov, N. Bakir, M. Bachmann, A. Gumenyuk, S. Na, M. Rethmeier, On the search for the origin of the bulge effect in high power laser beam welding, J. Laser Appl. 31(2) (2019) 022413.
[13] F. Lu, X. Li, Z. Li, X. Tang, H. Cui, Formation and influence mechanism of keyhole-induced porosity in deep-penetration laser welding based on 3D transient modeling, Int. J. Heat Mass Transf. 90 (2015) 1143-1152.
[14] M. Kern, P. Berger, H. Huegel, Magneto-fluid dynamic control of seam quality in CO2 laser beam welding. Weld. J. 79 (3) (2000), 72-78.
[15] V. Avilov, A. Fritzsche, M. Bachmann, A. Gumenyuk, M. Rethmeier, Full penetration laser beam welding of thick duplex steel plates with electromagnetic weld pool support, J. Laser Appl. 28 (2) (2016) 022420.
[16] A. Fritzsche, K. Hilgenberg, F. Teichmann, H. Pries, K. Dilger, M. Rethmeier, Improved degassing in laser beam welding of aluminum die casting by an electromagnetic field, J. Mater. Process. Technol. 253 (2018) 51-56.
[17] R. Chen, C. Wang, P. Jiang, X. Shao, Z. Zhao, Z. Gao, C. Yue. Effect of axial magnetic field in the laser beam welding of stainless steel to aluminum alloy. Mater. Des. 109 (2019) 146-152.

[18] Z. Zhu, X. Ma, C. Wang, G. Mi, G. Altering morphological, crystalline and compositional features in 316 L laser-MIG weldments with an external magnetic field, Mater. Des. 196 (2020) 109156.
[19] M. Gatzen, Influence of low-frequency magnetic fields during laser beam welding of aluminium with filler wire, Phys. Procedia 39 (2012) 59-66.
[20] X. Meng, M. Bachmann, A. Artinov, M. Rethmeier, Experimental and numerical assessment of weld pool behavior and final microstructure in wire feed laser beam welding with electromagnetic stirring, J. Manu. Process. 45 (2019) 408-418.
[21] Ö. Üstündağ, V. Avilov, A. Gumenyuk, M. Rethmeier, Improvement of filler wire dilution using external oscillating magnetic field at full penetration hybrid laser-arc welding of thick materials. Metals, 9(5) (2019) 594.
[22] M. Gatzen, Z. Tang, F. Vollertsen, M. Mizutani, S. Katayama, X-ray investigation of melt flow behavior under magnetic stirring regime in laser beam welding of aluminum, J. Laser Appl. 23 (3) (2011) 032002.
[23] B. Zhu, G. Zhang, J. Zou, N. Ha, Q. Wu, R. Xiao, Melt flow regularity and hump formation process during laser deep penetration welding. Opt. Laser Technol. 139 (2021) 106950.
[24] Y. Wang, P. Jiang, J. Zhao, S. Geng, Effects of energy density attenuation on the stability of keyhole and molten pool during deep penetration laser welding process: A combined numerical and experimental study. Int. J. Heat Mass Transf. 176 (2021) 121410.
[25] Y. Rong, J. Xu, H. Cao, H. Zheng, Y. Huang, G. Zhang, Influence of steady magnetic field on dynamic behavior mechanism in full penetration laser beam welding, J. Manu. Process. 26 (2017) 399-406.
[26] Ö. Üstündağ, N. Bakir, A. Gumenyuk, M. Rethmeier, Influence of oscillating magnetic field on the keyhole stability in deep penetration laser beam welding. Opt. Laser Technol. 135 (2021) 106715.
[27] L. Huang, P. Liu, S. Zhu, X. Hua, S. Dong, Experimental research on formation mechanism of porosity in magnetic field assisted laser welding of steel. J. Manu. Process. 50 (2020) 596-602.
[28] M. Bachmann, V. Avilov, A. Gumenyuk, M. Rethmeier, About the influence of a steady magnetic field on weld pool dynamics in partial penetration high power laser beam welding of thick aluminium parts, Int. J. Heat Mass Transf. 60 (2013) 309-321.
[29] M. Bachmann, V. Avilov, A. Gumenyuk, M. Rethmeier, Experimental and numerical investigation of an electromagnetic weld pool support system for high power laser beam welding of austenitic stainless steel, J. Mater. Process. Technol. 214 (2014) 578-591.

[30] M. Bachmann, V. Avilov, A. Gumenyuk, M. Rethmeier, Numerical simulation of full-penetration laser beam welding of thick aluminium plates with inductive support, J. Phys. D-Appl. Phys. 45 (3) (2011) 035201.
[31] J. Chen, Y. Wei, X. Zhan, Q. Gao, D. Zhang, X. Gao, Influence of magnetic field orientation on molten pool dynamics during magnet-assisted laser butt welding of thick aluminum alloy plates, Opt. Laser Technol. 104 (2018) 148-158.
[32] J. Chen, Y. Wei, X. Zhan, C. Gu, X. Zhao, Thermoelectric currents and thermoelectric-magnetic effects in full-penetration laser beam welding of aluminum alloy with magnetic field support, Int. J. Heat Mass Transf. 127 (2018) 332-344.
[33] R. Zhang, X. Tang, L. Xu, F. Lu, H. Cui, Mechanism study of thermal fluid flow and weld root hump suppression in full penetration laser welding of Al alloy with alternating magnetic field support, Int. J. Heat Mass Transf. 166 (2021) 120759.
[34] F. X. Chen, M. Luo, R. Hu, R. Li, L. Liang, S. Pang, Thermo-electromagnetic effect on weld microstructure in magnetically assisted laser welding of austenite steel, J. Manu. Process. 41 (2019) 111-118.
[35] M. Gatzen, Z. Tang, F. Vollertsen, Effect of electromagnetic stirring on the element distribution in laser beam welding of aluminium with filler wire, Phys. Procedia 12 (2011) 56-65.
[36] X. Meng, A. Artinov, M. Bachmann, M. Rethmeier, Theoretical study of influence of electromagnetic stirring on transport phenomena in wire feed laser beam welding. J. Laser Appl. 32 (2) (2020) 022026.
[37] X. Meng, A. Artinov, M. Bachmann, M. Rethmeier, Numerical and experimental investigation of thermo-fluid flow and element transport in electromagnetic stirring enhanced wire feed laser beam welding. Int. J. Heat Mass Transf. 144 (2019) 118663.
[38] X. Meng, M. Bachmann, A. Artinov, M. Rethmeier, The influence of magnetic field orientation on metal mixing in electromagnetic stirring enhanced wire feed laser beam welding, J. Mater. Process. Technol. 294 (2021) 117135.
[39] M. Bachmann, X. Meng, A. Artinov, M. Rethmeier, Elucidation of the Bulging Effect by an Improved Ray-Tracing Algorithm in Deep Penetration Wire Feed Laser Beam Welding and Its Influence on the Mixing Behavior. Adv. Eng. Mater. (2022) 2101299.
[40] D. L. Youngs, An interface tracking method for a 3D Eulerian hydrodynamics code, AWRE Technical Report, 44 (92) (1984) 35.
[41] J. U. Brackbill, D. B. Kothe, C. Zemach, A continuum method for modeling surface tension. J. Comput. Phys. 100 (2) (1992) 335-354.

[42] J. H. Cho, S. J. Na, Implementation of real-time multiple reflection and Fresnel absorption of laser beam in keyhole, J. Phys. D-Appl. Phys. 39 (24) (2006) 5372.
[43] S. W. Han, J. Ahn, S. J. Na, A study on ray tracing method for CFD simulations of laser keyhole welding: progressive search method, Weld. World, 60 (2) (2016) 247-258.
[44] J. L. Zou, S. K, Wu, W. X. Yang, Y. He, R. S. Xiao. A novel method for observing the micro-morphology of keyhole wall during high-power fiber laser welding, Mater. Des. 89 (2016) 785-790.
[45] V. Semak, A. Matsunawa, The role of recoil pressure in energy balance during laser materials processing. J. Phys. D-Appl. Phys. 30 (18) (1997) 2541.
[46] D. Peckner, I. Bernstein, Handbook of Stainless Steels, first ed., McGraw-Hill Book Company, New York, 1977.
[47] K. C. Mills, Recommended values of thermophysical properties for selected commercial alloys, first ed., Woodhead Publishing, Cambridge, 2002.
[48] K. D. Maglić, N. L. Perović, A. M. Stanimirović, Calorimetric and transport properties of Zircalloy 2, Zircalloy 4, and Inconel 625, Int. J. Thermophys. 15 (4) (1994) 741-755.40
[49] S. Muhammad, S. W. Han, S. J. Na, A. Gumenyuk, M. Rethmeier, Study on the role of recondensation flux in high power laser welding by computational fluid dynamics simulations, J. Laser Appl. 30 (1) (2018) 012013.
[50] A. Artinov, N. Bakir, M. Bachmann, A. Gumenyuk, M. Rethmeier, Weld pool shape observation in high power laser beam welding. Procedia CIRP 74 (2018) 683-686
[51] W. I. Cho, S. J. Na, C. Thomy, F. Vollertsen, Numerical simulation of molten pool dynamics in high power disk laser welding, J. Mater. Process. Technol. 212 (2012) 262-275.
[52] Y. Kawahito, K. Nakada, Y. Uemura, M. Mizutani, K. Nishimoto, H. Kawakami, S. Katayama, Relationship between melt flows based on three-dimensional X-ray transmission in situ observation and spatter reduction by angle of incidence and defocussing distance in high-power laser welding of stainless steel, Weld. Int. 32 (7) (2018) 485-496.
[53] D. Zhang, M. Wang, C. Shu, Y. Zhang, D. Wu, Y. Ye, Dynamic keyhole behavior and keyhole instability in high power fiber laser welding of stainless steel, Opt. Laser Technol. 114 (2018) 1-9.
[54] R. Lin, H. P. Wang, F. Lu, J. Solomon, B. E. Carlson, Numerical study of keyhole dynamics and keyhole-induced porosity formation in remote laser welding of Al alloys, Int. J. Heat Mass Transf. 108 (2017) 244-256.
[55] M. Wu, A. Vakhrushev, G. Nummer, C. Pfeiler, A. Kharicha, A. Ludwig, Importance of melt flow in solidifying mushy zone, Open Transp. Phenom. J. 2 (2010) 16-23.

[56] W. Huang, H. Wang, T. Rinker, W. Tan, Investigation of metal mixing in laser keyhole welding of dissimilar metals, Mater. Des. 195 (2020) 109056.
[57] L. J. Zhang, J. X. Zhang, A. Gumenyuk, M. Rethmeier, S. J. Na, Numerical simulation of full penetration laser welding of thick steel plate with high power high brightness laser, J. Mater. Process. Technol. 214 (8) (2014) 1710-1720.